

Spin wave generation by surface acoustic waves

Xu Li,¹ Dominic Labanowski,² Sayeef Salahuddin,² and Christopher S. Lynch¹

¹*Department of Mechanical and Aerospace Engineering, University of California, Los Angeles, California 90095, USA*

²*Department of Electrical Engineering and Computer Sciences, University of California, Berkeley, California 94720, USA*

(Received 18 April 2017; accepted 14 July 2017; published online 27 July 2017)

Surface acoustic waves (SAW) on piezoelectric substrates can excite spin wave resonance (SWR) in magnetostrictive films through magnetoelastic coupling. This acoustically driven SWR enables the excitation of a single spin wave mode with an in-plane wave vector k matched to the magnetoelastic wave vector. A 2D frequency domain finite element model is presented that fully couples elastodynamics, micromagnetics, and piezoelectricity with interface spin pumping effects taken into account. It is used to simulate SAW driven SWR on a ferromagnetic and piezoelectric heterostructure device with an interdigital transducer configuration. These results, for the first time, present the spatial distribution of magnetization components that, together with elastic wave, exponentially decays along the propagation direction due to magnetic damping. The results also show that the system transmission rate $S_{21}(\text{dB})$ can be tuned by both an external bias field and the SAW wavevector. Acoustic spin pumping at magnetic film/normal metal interface leads to damping enhancement in magnetic films that decreases the energy absorption rate from elastic energy. This weakened interaction between the magnetic energy and elastic energy leads to a lower evanescence rate of the SAW that results in a longer distance propagation. With strong magnetoelastic coupling, the SAW driven spin wave is able to propagate up to $1200\text{ }\mu\text{m}$. The results give a quantitative indication of the acoustic spin pumping contribution to linewidth broadening. *Published by AIP Publishing.* [<http://dx.doi.org/10.1063/1.4996102>]

I. INTRODUCTION

Control of a single spin wave mode and achieving a long spin wave travelling distance in micron to millimeter scale structures is of great interest for spintronic device applications. Over the past few years, spin wave propagation has been subject to intense research activity for its potential application in next-generation logic devices and spintronics. Considerable effort has been directed toward spin wave generation and propagation methods such as through Dzyaloshinskii-Moriya interactions,^{1,2} using magnetic domain walls as reconfigurable spin-wave nanochannels,³ and propagating spin waves in a microstructured magnonic crystals.⁴ Due to intrinsic spin relaxation, spin waves generally decay within several micrometers in metals.^{1,4}

Recent works have focused on acoustically driven spin wave resonance (SWR) in multiferroic systems.^{5–11} This is achieved through magnetoelastic coupling. Magnetoelastic coupling is a function of the distance between spins affecting exchange interaction, magnetic dipole-dipole interaction, and spin-orbit interaction.¹² Mechanical waves have much smaller damping than spin waves and thus can assist spin wave propagation through magnetoelastic coupling.¹³ Surface acoustic wave (SAW) driven SWR devices provide high selectivity of spin wave modes with an in-plane wave vector modulated by SAW. This enables the deterministic control of the resonance frequency for spintronic device design. Compared to electric current induced magnetic field excitations of SWR, SAWs represent an energy efficient voltage driven SWR generation method. Analytical works addressing the coupling of micromagnetics and elasticity

have been performed for acoustically driven spin wave resonance system.^{10,14} Dynamic non-volatile magnetization switching by SAW was also investigated for the cases of perpendicular magnetized films¹⁵ and magnetostrictive nanoelements.¹⁶

The SAW driven SWR device investigated consists of a magnetostrictive element placed between two interdigital transducers (IDTs) on a single crystal piezoelectric substrate lithium niobate (LiNbO_3), as shown in Fig. 1. Electric power is sourced into the system through the input IDT, and a corresponding periodic elastic stress is established through the piezoelectric effect. A surface acoustic wave (SAW) is thus generated. The output IDT acts in a reciprocal manner, converting elastic energy into electrical energy. The SAW is generated at a frequency such that the wavelength is equal to the transducer pitch. When the SAW propagates through the magnetostrictive film, it interacts with the spin and excites the film into resonance if the SAW frequency matches the spin precession frequency. Acoustic waves and spin waves are thus coupled. The resulting coupled wave is called a magnetoelastic wave, and this SAW driven SWR phenomenon is called magnetoelastic resonance.¹² The inset in Fig. 1 is an illustration of spin pumping occurring at the magnetic film/normal metal (M/NM) interface.

SAW driven SWR devices that use this configuration have been experimentally demonstrated.^{5,6,10,11} Most of the experiments produced a four-fold symmetry in an energy absorption rate diagram by parametrically sweeping the angle θ that an equilibrium magnetization makes with respect to the SAW propagation direction. A maximum

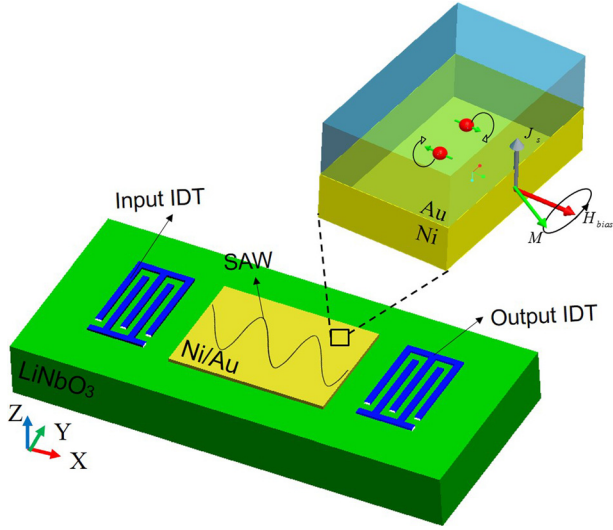


FIG. 1. SAW driven SWR device set up with SAW propagating along x axis. The inset shows spin pumping occurring at the M/NM interface.

absorption rate occurred when $\theta = (2n + 1)\frac{\pi}{4}$, so the magnetic film biased along 45° away from the SAW propagation direction produces the largest damping of the SAW.^{5,6,11,14} In the experiments, a broadening linewidth of the resonance spectrum due to damping enhancement in the ferromagnetic thin film was also observed,^{5,11,14} but the reasons for this were not identified. In this work, a systematic frequency-dependent study of the SAW-SWR system was conducted to determine the frequency-dependent nonlinear dynamic susceptibility spectrum for a magnetic thin film. A spin wave and elastic wave were fully coupled by the magnetostrictive strain in a lithium niobate substrate. This enabled capturing the acoustic spin pumping effect occurring at the M/NM interface. These effects were shown to contribute to the linewidth broadening.

In the work presented below, a frequency domain FEA model was used that fully couples micromagnetics, piezoelectricity, and elastodynamics with a feedback magnetostriction strain term from the magnetic system to the elastic system implemented. The frequency domain model provides a method to simulate the fully coupled multiphysics for spintronic and radio frequency (RF) devices. Next, the frequency-dependent nonlinear dynamic susceptibility was analyzed with a micromagnetics simulation that captures the high frequency dynamics of magnetic materials. Acoustic spin pumping was implemented in the code as a boundary torque rather than using a homogeneous macro-spin model. This enabled simulation of the spin relaxation behavior at the M/NM interface at ferromagnetic resonance (FMR) as well as at a higher order spin wave resonance mode. This fully coupled finite element model provided insight into the underlying physics of SAW driven SWR devices.

II. THEORY

The multiphysics model couples micromagnetics, elastodynamics, and linear piezoelectricity. Micromagnetics describes the damped spin behavior in a magnetic field and

is described by the Landau–Lifshitz–Gilbert (LLG) equation¹⁷ in the time domain

$$\frac{\partial \underline{M}}{\partial t} = -\mu_0 \gamma \underline{M} \times \underline{H}_{eff} + \frac{\alpha}{M_s} \underline{M} \times \frac{\partial \underline{M}}{\partial t}, \quad (1)$$

where μ_0 is the vacuum permeability, γ is the gyromagnetic ratio, α is the Gilbert damping constant, \underline{M} is magnetization, M_s is saturation magnetization, \underline{H}_{eff} is total effective field, which includes an external bias field H_{ext} , magnetostatic field (demagnetization field) H_{demag} , exchange field H_{ex} , and magnetoelastic field H_{me} .

The LLG equation in the frequency domain was obtained by assuming time harmonic motion of the spin in an excitation field, where the magnetization is expressed as $\underline{M} = \underline{M}_{eq} + \underline{\delta m}(x, \omega)e^{i\omega t}$, where \underline{M}_{eq} is equilibrium magnetization, $\underline{\delta m}(x, \omega)$ is the magnetization deviation, and ω is the angular frequency. Note that the spatially varying components of the spin wave are contained in $\underline{\delta m}(x, \omega)$ since it is calculated at each mesh node, which denotes different spatial/geometry points. It is equivalent to the analytical expression $\underline{\delta m}(x, \omega) = \underline{\delta m}_0(\omega)e^{-ikx}$, where $\underline{\delta m}_0$ is a frequency-dependent term and k is the spin wave wave-vector. The magnetic field is expressed as $\underline{H}_{eff} = \underline{H}_{eq} + \underline{\delta h}e^{i\omega t} + \underline{H}_T(\underline{\delta m})$, where \underline{H}_{eq} is equilibrium magnetic field and $\underline{\delta h}$ is the excitation field. Here, $\underline{\delta h}$ represents the magnetoelastic field. $\underline{H}_T(\underline{\delta m})$ is the effective magnetic field change due to the magnetization deviation $\underline{\delta m}$. The LLG equation is linearized for magnetization motion around its equilibrium state to compute its linear magnetization response $\underline{\delta m}$ under a weak external excitation field $\underline{\delta h}$.¹⁸ Although the LLG equation is linear at a given frequency, the relationship between magnetization and excitation field is non-linear with frequency and represented by the susceptibility being dependent on frequency. Equation (1) is linearized in the frequency domain as Eq. (2)

$$i\omega \underline{\delta m} - (\gamma \mu_0 \underline{H}_{eq} + i\alpha \omega \underline{m}_{eq}) \times \underline{\delta m} + \gamma \mu_0 \underline{m}_{eq} \times \underline{H}_T(\underline{\delta m}) = -\gamma \mu_0 \underline{m}_{eq} \times \underline{\delta h}. \quad (2)$$

Three math operators are introduced, \underline{D}_1 , \underline{D}_2 , and \underline{D}_3 , which are defined as $\underline{D}_1 \underline{\delta m} = \mu_0 |\gamma| \underline{m}_{eq} \times \underline{\delta m}$, $\underline{D}_2 \underline{\delta m} = (|\gamma| \mu_0 \underline{H}_{eq} + i\alpha \omega \underline{m}_{eq}) \times \underline{\delta m}$, and $\underline{D}_3 \underline{\delta m} = \underline{H}_T(\underline{\delta m})$, respectively. Then, by introducing these three tensors, Eq. (2) can be rearranged to give the following equation:¹⁸

$$\underline{\delta m} = -\left(i\omega \underline{I} - \underline{D}_2 + \underline{D}_1 \underline{D}_3\right)^{-1} \underline{D}_1 \underline{\delta h} = \underline{\chi}(\omega) \underline{\delta h}, \quad (3)$$

where $\underline{\chi}(\omega)$ is a 2nd order dynamic susceptibility tensor that determines the amplitude of the magnetic response. Note that although \underline{D}_2 linearly depends on frequency, the inverse of $i\omega \underline{I} - \underline{D}_2 + \underline{D}_1 \underline{D}_3$ is non-linear. Therefore, the dependence of susceptibility on frequency is non-linear. \underline{I} is a 2nd order unit tensor, and $i = \sqrt{-1}$. Equation (3) describes the linear response of magnetic materials to an oscillating

excitation field at a given frequency. Specifics of the \underline{D}_1 , \underline{D}_2 , and \underline{D}_3 tensors are given in [Appendix A](#).

The behavior of the single crystal Y-Z cut lithium niobate follows linear piezoelectricity as described by Eqs. (4) and (5).¹⁹ Equations (6)–(8) describe elastodynamics in the magnetic layer²⁰

$$\underline{\underline{\sigma}} = \underline{\underline{C}}^E \underline{\underline{\varepsilon}}^{el} - \underline{\underline{e}} \underline{E}, \quad (4)$$

$$\underline{D} = \underline{\underline{e}}^T \underline{\underline{\varepsilon}}^{el} + \underline{\underline{\zeta}} \underline{E}, \quad (5)$$

$$-\rho \omega^2 \underline{u} = \nabla \cdot \underline{\underline{\sigma}}, \quad (6)$$

$$U_{me} = \frac{B_1}{M_s^2} \sum_p M_p^2 \varepsilon_{pp}^{tot} + \frac{B_2}{M_s^2} \sum_p \sum_{q \neq p} M_p M_q \varepsilon_{pq}^{tot}, \quad (7)$$

$$\underline{\underline{\varepsilon}}^{el} = \underline{\underline{\varepsilon}}^{tot} - \underline{\underline{\varepsilon}}^f = \frac{1}{2} [(\nabla \underline{u})^T + \nabla \underline{u}] - \underline{\underline{\varepsilon}}^f, \quad (8)$$

where ρ is the material density, \underline{u} is the displacement field, $\underline{\underline{\sigma}}$ is the stress tensor, $\underline{\underline{\varepsilon}}^{tot}$ is the total strain tensor, $\underline{\underline{\varepsilon}}^{el}$ is the elastic strain tensor, $\underline{\underline{\varepsilon}}^f$ is a feedback magnetostriction strain term ([Appendix A](#)), U_{me} is the magnetoelastic energy, B_1 and B_2 are the magnetoelastic constants, \underline{D} is the electric displacement, and \underline{E} is the electric field. $\underline{\underline{C}}^E$ is the elastic stiffness tensor measured under constant E . $\underline{\underline{\zeta}}$ is the permittivity tensor. $\underline{\underline{e}}$ is the piezoelectric coupling tensor. A piezoelectric Rayleigh wave is used for Y-Z cut lithium niobate in the simulation, which is similar to the Rayleigh wave for an isotropic material but modified with anisotropy and piezoelectricity in a half space. A fully coupled magnetoelastic wave function for frequency-dependent magnetization oscillation is implemented into the model. Parameters for Y-Z cut lithium niobate are given in [Appendix B](#).

When a ferromagnetic material is capped with a normal metal layer, magnetization dynamics induces spin pumping at the interface that absorbs spin angular momentum and enhances damping in the magnetic layer. The angular momentum loss is a form of spin current injected into the metal layer. Its frequency domain expression is given by the following equation:²¹

$$\underline{I}_s = \frac{\hbar \gamma}{M_s} \left(\text{Re} [g_{\uparrow\downarrow}^r - g_{\uparrow\downarrow}^t] \underline{m} \times i \omega \underline{m} + \text{Im} [g_{\uparrow\downarrow}^r - g_{\uparrow\downarrow}^t] i \omega \underline{m} \right) \delta \left(z - \frac{L}{2} \right), \quad (9)$$

where \underline{I}_s is the spin current. $g_{\uparrow\downarrow}^r$ and $g_{\uparrow\downarrow}^t$ are the complex reflection and transmission spin mixing conductance per unit contact area, \hbar is the reduced Planck's constant, z is the global Cartesian coordinate normal to the device surface, and L is the thickness of the Ni film. For a thin film, it can be further reduced to the following equations:²²

$$\underline{I}_s \simeq \frac{\hbar \gamma}{M_s} (\text{Re} [g_{\uparrow\downarrow}^r] \underline{m} \times i \omega \underline{m}) \delta \left(z - \frac{L}{2} \right), \quad (10)$$

$$\underline{I}_c = \alpha_{SH} \left(\frac{2e}{\hbar} \right) (\hat{e}_s \times \underline{I}_s), \quad (11)$$

where I_c is the electric current, α_{SH} is the spin Hall angle for Au, and e is the electron charge. The boundary for the magnetic film should fulfill the zero total surface torque condition given by the following equation:²³

$$\underline{T}_{surf} + \underline{T}_{ex} + \underline{T}_{sp} = 0, \quad (12)$$

$$\underline{T}_{surf} = \frac{2\gamma K_s}{M_s} (\underline{M} \times M_3 \hat{e}_3), \quad (13)$$

$$\underline{T}_{ex} = -\mu_0 \gamma \left[\frac{2A_{ex}}{\mu_0 M_s} \underline{M} \times \frac{\partial \underline{M}}{\partial n} \right], \quad (14)$$

$$\underline{T}_{sp} = \frac{\hbar \gamma}{M_s} \text{Re} [g_{\uparrow\downarrow}^r] \underline{M} \times (i \omega) \underline{M}, \quad (15)$$

where T_{surf} , T_{ex} , and T_{sp} are magnetic torques induced by surface anisotropy, exchange interaction, and spin pumping, respectively, K_s is the surface anisotropy constant, and A_{ex} is exchange stiffness. Note that the surface anisotropy torque T_{surf} was included in the simulation in order to investigate its influence on the system, though it turned out to be negligible in these simulations. It is because M_3 is almost zero in the magnetic film due to the in-plane equilibrium magnetization state. Spin pumping was implemented in all of the simulation work presented below. In the last part of Sec. III, additional scenarios regarding spin pumping are presented in order to elucidate its effect on SAW and spin wave propagation. Critical coefficients used in the simulations are given in [Table I](#).

III. RESULTS

The theory summarized in Sec. II was implemented in a frequency domain finite element model. The SAW driven SWR device shown in [Fig. 1](#) was simulated using the FEA model. The geometry and materials consisted of two aluminum IDTs on Y-Z cut lithium niobate aligned with the SAW propagation direction. The SAW velocity for this material is 3488 m/s.¹⁹ The periodicity of the IDTs was varied from 6.28 μm to 1.74 μm , which gives a fundamental operating

TABLE I. Critical coefficients used in the SAW driven SWR simulation.

Properties	Value
Saturation magnetization magnitude, M_s (Ref. 24)	4.8e5 (A/m)
Exchange stiffness constant, A (Ref. 24)	1.05×10^{-11} (J/m)
Surface anisotropy constant, K_s (Ref. 25)	1.5×10^{-4} (J/m ²)
Intrinsic damping coefficient, α (Ref. 24)	0.038
Bulk magneto-elastic coupling constant, B_1 (Ref. 24)	6.2×10^6 (J/m ³)
Bulk magneto-elastic coupling constant, B_2 (Ref. 24)	4.3×10^6 (J/m ³)
Reduced Planck constant \hbar (Ref. 24)	$1.054571800 \times 10^{-34}$ (J·s)
Spin Hall angle α_{SH} for Au (Refs. 26 and 27)	0.16 (rad)
Gyromagnetic ratio γ (Ref. 24)	1.760859×10^{11} [1/(s T)]

frequency from 555 MHz to 2000 MHz. The IDTs generate a SAW with a wave vector varying from $1 \text{ rad}/\mu\text{m}$ to $3.6 \text{ rad}/\mu\text{m}$. A magnetostrictive nickel thin film was placed between the two IDTs and a thin gold capping layer was used to prevent oxidation of the Ni film. The Ni film width was varied from $200 \mu\text{m}$ to $1200 \mu\text{m}$, and the thickness was either 25 nm or 50 nm . The overall device dimensions were $1.5 \text{ mm} \times 60 \mu\text{m}$. Perfectly matched layers were added at the device boundaries to prevent wave reflection. These configurations were used to investigate the SAW wave vector effect on the SWR spectrum of the magnetic thin film.

The first simulation was directed at investigating the effects of the bias field and SAW wave vector on the SWR spectrum characteristics and on the device transmission coefficient $S_{21}(\text{dB})$. Figure 2(a) shows the energy absorption rate phase diagram under an in-plane bias field along different directions, which was normalized by the maximum energy absorption rate. A wave vector of $k = 2 \text{ rad}/\mu\text{m}$ is used for this simulation. A flower petal shaped diagram was obtained. This indicates that the maximum energy absorption rate occurs when the applied magnetic field is at around a 45° direction away from the SAW propagating direction. A similar energy absorption rate diagram was observed in experiments.^{5,6,11,14} This phenomenon is the result of the maximum magnetoelastic torque occurring when the SAW wave vector makes a 45° with the equilibrium magnetization direction. For all the subsequent simulations presented below, the Ni film was magnetically initialized along the 45° direction by an external field. Figure 2(b) is a cross section view of a FEA simulation result showing the SAW propagating along the x-coordinate axis with wave vector $k = 3.6 \text{ rad}/\mu\text{m}$. The color indicates the magnitude of the ϵ_{11} -component of the strain field, and the red arrows indicate particle displacement. Figure 2(c) shows the bias field dependent SWR spectrum as a function of wave vector k . As k increases, a broadening linewidth and an increasing resonance bias field H_{res} are observed. Since the energy absorbed by the magnetic film is determined by¹⁴ $P_{\text{abs}} = -\frac{\omega\mu_0}{2} \iint_V \text{Im}[H_{\text{res}}^* \chi H_{\text{res}}] dV$, more

power absorption is expected as the resonance field increases due to the increasing wave vector k . Note that spin mixing conductance in this particular simulation was set to zero to show the magnetic thin film intrinsic resonance spectrum. Figure 2(d) shows the bias field dependent device transmission parameter $S_{21}(\text{dB})$ for different wave vectors. Larger wave vectors induce more power absorption by the magnetic film. A similar effect was observed in an experimental work.⁵ This indicates an increase in the elastic energy transferring into the magnetic energy of the system through magnetoelastic coupling. A resonance magnetic field shift in the S_{21} curves is also observed as the wave vector increases, resulting from the SWR spectrum shift seen in Fig. 2(c). Figure 2 illustrates that the SWR spectrum of the magnetic film and device transmission S_{21} can be tuned by both the SAW wave vector and the external bias field.

When the SAW propagates through the Ni film, the magnetoelastic torque induces a spin wave with a definite in-plane wave vector that is matched to the coupled magnetoelastic wave vector. Instead of a pure surface anisotropy field induced spin wave,²⁸ which has no resonance mode selectivity, this SAW driven SWR enables deterministic excitation of a spin wave mode. A frequency-domain FEA simulation was run with a SAW wave vector $1.2 \text{ rad}/\mu\text{m}$, bias field 520 A/m and electric field $1\text{e}5 \text{ V/m}$ applied to the substrate. Continuous power was provided to the input IDT to obtain the steady-state response of the system in the frequency domain. The frequency domain finite element solution only provides the steady state response after resonance has been fully excited. Figure 3 shows the real part of longitudinal acoustic wave ϵ_{11} component along the SAW propagation direction for 25 nm Ni thick films with a length of $200 \mu\text{m}$, $600 \mu\text{m}$, and $1200 \mu\text{m}$, respectively. Mechanical damping rate for lithium niobate is in the range of 0.02 to 0.2 dB/mm depending on the crystal cut, operation frequency, and measure temperature.^{29–31} This is much smaller than the energy exchange induced damping rate of 23 dB/mm extracted from Fig. 3. Therefore, in this work, mechanical

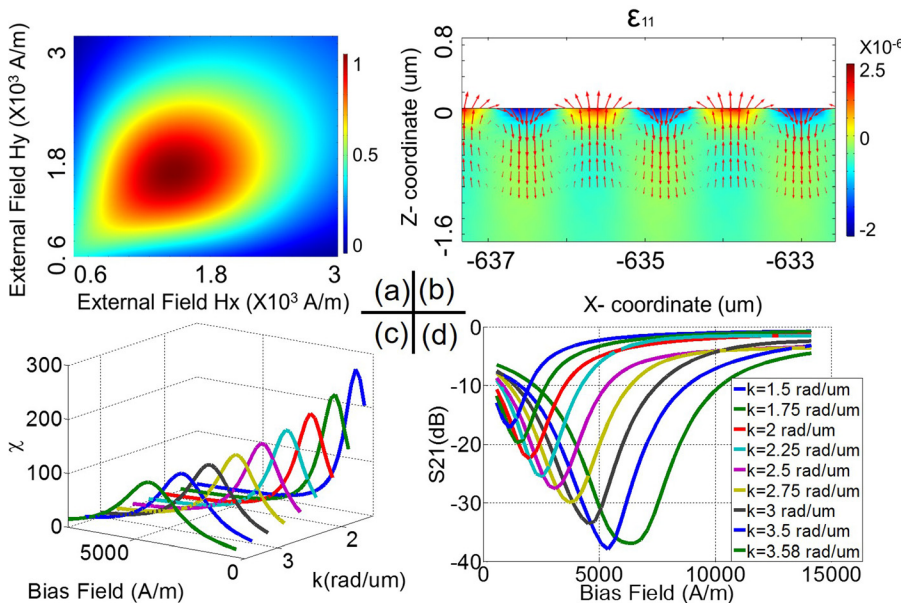


FIG. 2. (a) Normalized energy absorption rate phase diagram under different bias fields. (b) Cross-sectional view of 11 component of strain field with wave vector $k = 3.6 \text{ rad}/\mu\text{m}$. Red arrows indicate particle displacement. (c) Bias field dependent SWR spectrum under different wave vectors. (d) Bias field dependent device transmission $S_{21}(\text{dB})$ under different wave vectors.

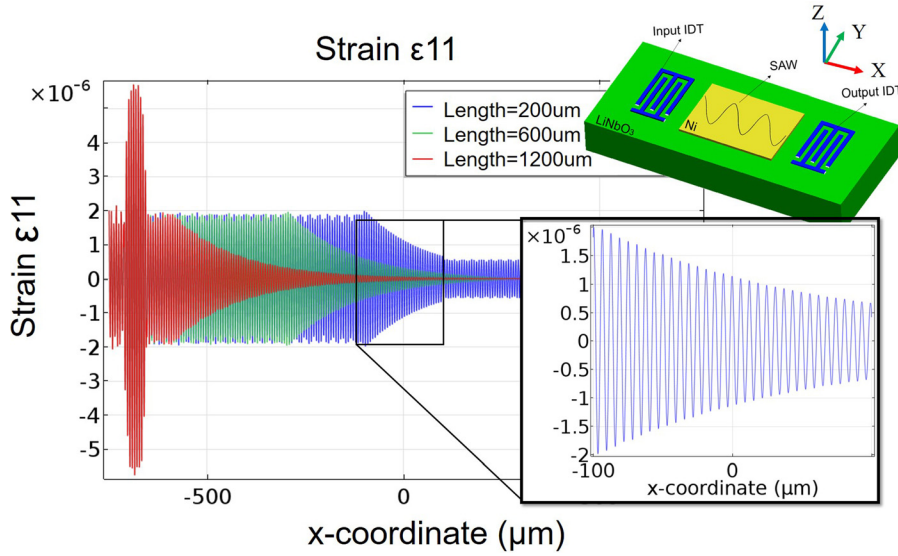


FIG. 3. Travelling elastic wave 11 component ($k = 1.2 \text{ rad}/\mu\text{m}$) along x coordinate for $200 \mu\text{m}$, $600 \mu\text{m}$ and $1200 \mu\text{m}$ magnetic film, respectively. The inset shows the close-up of the SAW for the $200 \mu\text{m}$ magnetic film. An exponential decay occurs when SAW propagates through magnetic film. Input IDT is located at $-700 \mu\text{m}$, where the localized strain maxima is observed.

damping rate is neglected. In Fig. 3, the elastic wave exhibits an exponential decay when it propagates past the Ni film due to the feedback magnetostrictive strain from the magnetic system. The inset is a close-up of the SAW in the $200 \mu\text{m}$ film. The corresponding excited spin wave in this film is shown in Fig. 4. Figure 4(a) shows the real part of the three magnetization deviation components, δm_1 , δm_2 , and δm_3 . Due to intrinsic magnetic damping, the spin wave usually damps out much more quickly than acoustic wave,¹³ which results in the spin wave amplitude being only determined by the local acoustic wave amplitude instead of the accumulated acoustic energy. The largest SAW amplitude, at the edge of magnetic film closest to the source, gives a maximum steady-state resonance amplitude of the spin wave. With the total energy gradually attenuated along the Ni film due to magnetic damping, evanescence of both the spin wave and SAW amplitude occur, as shown in Figs. 3 and 4. Spin pumping at the M/NM interface was taken into account in this simulation. Without the spin pumping effect, the attenuation rate becomes higher as discussed below. For better illustration of the spin wave, a small region is extracted from the whole magnetic film indicated by the dashed rectangle in Fig. 4(a) and plotted in Fig. 4(b). It shows that δm_1 and δm_2 are out-of-phase by 90° as expected, and due to a strong demagnetization field along the z axis, δm_3 is suppressed leading to a smaller amplitude compared with the other two. Figure 4(c) shows both the spin wave and elastic wave in the same extracted region. An identical wave vector for both spin wave and SAW wave is observed, which demonstrates the deterministic selectivity of the spin wave mode in a magnetic film matched to the magnetoelastic wave vector. This simulation result shows that a single spin wave excitation mode can be deterministically modulated by the SAW wave vector.

Another interesting phenomenon that has been reported in many SAW driven SWR experiments is damping enhancement in magnetic thin films,^{5,11,14} and the reason for it remained unclear. Several possible causes have been proposed, such as nonuniform excitation by SAW,¹⁴ a two magnon processes,¹⁴ and spin pumping.¹¹ Spin pumping occurs at the M/NM interface, and this further induces an inverse

spin Hall effect (ISHE) in the metal layer by injecting spin current into it. This non-local interaction can induce damping enhancement in magnetic films. Some effort has been made in investigating the uniform spin pumping effect on

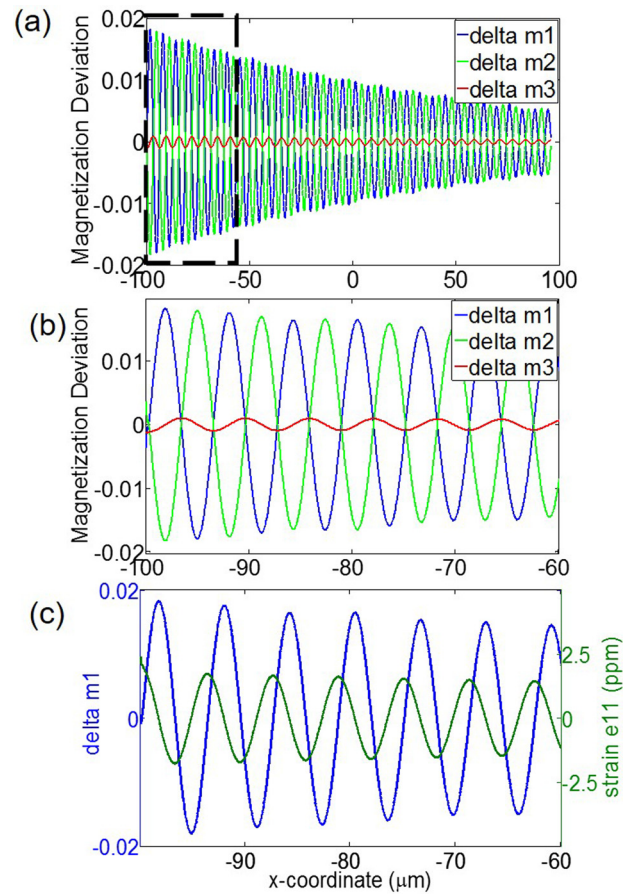


FIG. 4. (a) Spin wave for the $200 \mu\text{m}$ magnetic film along x coordinate driven by SAW with $k = 1.2 \text{ rad}/\mu\text{m}$. Three components of magnetization deviation, δm_1 , δm_2 , and δm_3 are presented. (b). Close-up of the spin wave as indicated by the dashed rectangular in (a). δm_1 and δm_2 are out-of-phase by 90° . Due to a strong demagnetization field along the z axis, δm_3 is suppressed leading to a smaller amplitude compared with the other two. (c). Spin wave and elastic wave in the same extracted region. The two waves have identical wave vectors.

this damping enhancement by using a “macrospin” model and a negative conclusion was obtained by showing that uniform spin pumping can only increase the damping factor by about 0.006 for Ni film.¹¹ However, a “macrospin” excitation, commonly referred as the FMR mode, is only one of many types of magnetic resonance excitation in magnetic thin films. It has been demonstrated experimentally³² and analytically²² that non-uniform excitation modes in magnetic films can behave differently from the FMR mode in terms of spin pumping, and different magnetoelastic wave propagation directions also impact the spin pumping effect.³³

In order to more accurately describe nonuniform spin pumping behavior in the Ni film, an acoustic spin pumping model was implemented to explore its effect on damping enhancement. Acoustic spin pumping is driven by the voltage-induced acoustic wave in the piezoelectric substrate, which interacts with spins in the magnetic layers and thus induces spin pumping at the magnetic/metal interface.^{34,35} Because acoustic spin pumping arises from a surface spin wave that is induced by the presence of a surface anisotropy torque, surface exchange interaction torque and spin pumping torque together, it was implemented as a boundary torque rather than as an average of the spin pumping effect through the whole film. The inset in Fig. 1 is an illustration of spin pumping occurring at Ni/Au interface. A spin current is pumped into the Au layer by the precessing magnetic moments in the Ni film. Due to the ISHE, the spin-polarized current induces an electric current that accumulates electrical charges with opposite signs at the opposite lateral surfaces. This effect leads to an electric signal that can be measured through an external analog circuit terminal.²⁶ Two parameters are critical in analyzing spin pumping,²² spin mixing conductance $g_{\uparrow\downarrow}$, and spin Hall angle α_{SH} . However, no available value for spin mixing conductance at the Ni/Au interface was available. A value range of $1 \times 10^{15} - 1 \times 10^{17} \frac{1}{\text{cm}^2}$ depending on the spin Hall angle of metal layer is given by Zink’s calculation work on ISHE for native oxides of nickel and permalloy with platinum and gold overlayers.²⁶ A spin Hall angle α_{SH} 0.0016 (rad) for Au is commonly used in the literature.^{26,27} Therefore, a median value of spin mixing conductance, $1 \times 10^{16} \frac{1}{\text{cm}^2}$, was chosen for the FEA simulation. Figure 5(a) shows a film size dependent transmission S_{21} (dB). Four sets of data are displayed, experimental results (black square),⁶ FEA simulation results for intrinsic damping 0.038 without acoustic spin pumping (red dot), intrinsic

damping 0.038 with acoustic spin pumping (blue upward triangle), and equivalent effective damping factor $\alpha' = 0.13$ (pink downward triangle). A SAW wave vector $k = 3.58 \text{ rad}/\mu\text{m}$ was chosen for this simulation in order to compare with experimental results.⁶ In Ref. 6, the system transmission rate S_{21} (dB) was measured for three different film lengths. These experimental data are compared with simulation results. Figure 5(a) shows that with intrinsic damping of 0.038, the SAW almost completely damps out after it propagates $400 \mu\text{m}$ past the magnetic film (red dots). Since the spin wave is strongly coupled to the SAW, if the SAW almost completely damps out at $400 \mu\text{m}$, there is almost no significant energy exchange between the elastic system and magnetic system after this propagation distance. Due to intrinsic magnetic damping, spin waves can only continue to propagate up to several micrometers in metals.^{1,4,13} Therefore, it is reasonable to assume that the spin wave almost completely damps out together with the SAW at around $400 \mu\text{m}$ in this case. The experimental results⁶ indicate a much lower energy exchange rate, which enables the SAW and spin wave to propagate up to $1200 \mu\text{m}$ (black squares). This gives an equivalent damping factor of 0.13 in the magnetic film (pink downward triangle), which is approximately three times the intrinsic Gilbert damping 0.038. This damping factor dependent energy exchange rate can be better explained by Fig. 5(b). Figure 5(b) shows the FMR spectrum (imaginary part of susceptibility) with various damping factors of Ni film under the same bias field 5656 A/m. This figure demonstrates that the susceptibility of the magnetic film has a non-linear dynamic dependence on frequency. As the damping factor increases, a decrease in the susceptibility was observed together with a linewidth broadening phenomenon. Since energy absorption rate in Ni film is expressed as $P_{\text{abs}} = -\frac{\omega\mu_0}{2} \iint \text{Im}[H_{\text{bias}}^* \chi H_{\text{bias}}] dV$,¹⁴ a decrease in susceptibility χ leads to a lower energy absorption rate. Spin pumping induces additional damping, approximately 0.09, in the magnetic film [Fig. 5(a), blue upward triangles] and thus decreases its energy absorption rate from elastic energy. A lower evanescence rate of the SAW is obtained from its reduced interaction with the spin wave because the spin wave loses its momentum to the metal layer as a form of spin current. On the contrary, without spin pumping induced additional damping, the spin wave has a higher resonance amplitude, which enhances its energy absorption rate from elastic energy and thus increases the evanescence rate of SAW. Therefore, the

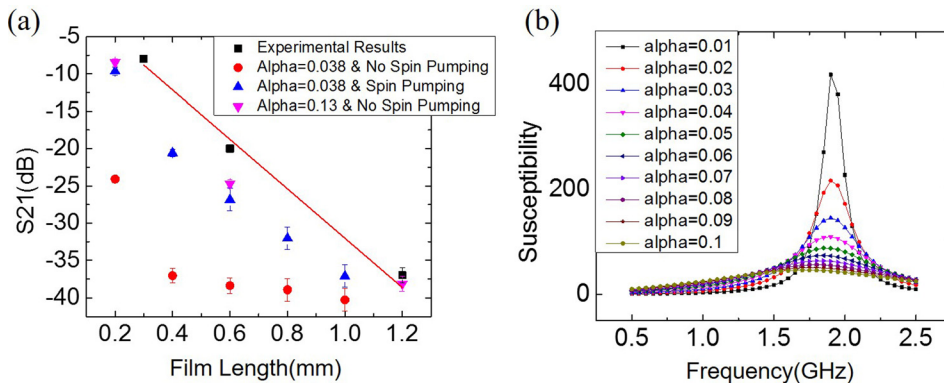


FIG. 5. (a) Transmission S_{21} (dB) as a function of film length under 5656 A/m bias field. Four data sets are presented, experimental data(black square), simulation results for intrinsic damping 0.038 without spin pumping(red dot), intrinsic damping 0.038 with spin pumping(blue upward triangle) and equivalent effective damping factor 0.13 without spin pumping(pink downward triangle). Linear fit is given for experimental data. (b) Susceptibility spectrum with various damping factors under 5656 A/m bias field.

spin wave can propagate farther with a lower evanescence rate due to spin pumping. In this simulation, all data sets were evaluated at the same bias field of 5656 A/m to study the spin pumping effect on a SAW-SWR device with a fixed IDT configuration. The mesh size was reduced until there was less than a 1% error for the energy absorption rate. Error bars of this magnitude are shown in Fig. 5(a). The error bars shown for the experimental data are estimated from two different experimental set-ups on the same device that were tested with almost identical S_{21} (dB) energy absorption rate. The fabrication error in the electrical pad size could result in just 1.7% error for the worst case in 300 μm film. This percentage of error is reflected in Fig. 5(a). Note that the spin mixing conductance at the Ni/Au interface was merely estimated from the previous analytical work.²⁶ The real mixing conductance in the experiments could be either higher or lower. A higher spin mixing conductance constant will result in more damping enhancement in the Ni film, which thus lowers the evanescence rate of the SAW, and vice versa. Nevertheless, the computational results in this work still provide a convincing argument that acoustic spin pumping is one of main mechanisms responsible for linewidth broadening phenomenon.

IV. CONCLUSION

A frequency-domain 2D finite element model was developed that fully couples micromagnetics, piezoelectrics, and elastodynamics with a spin pumping effect at the M/NM interface and was used to simulate a SAW driven SWR device that generates spin waves with selective resonance modes. The simulation results showed that the characteristics of the SWR spectrum and device transmission S_{21} (dB) can be tailored by both bias magnetic field and SAW wave vector. Using the fully coupled FEA code, a spatial distribution of spin waves and elastic waves was shown in this work that indicated an exponential decay along the SAW propagation direction. Spin pumping at the M/NM interface causes damping enhancement in the magnetic film which lowers its energy absorption rate from elastic energy. A lower evanescence rate of the SAW is thus observed due to its reduced interaction with the spin wave, which in turn enables a longer distance propagation of the spin wave (up to 1200 μm) in the magnetic film. These simulation results provide a persuasive explanation for the damping enhancement phenomenon observed by experimentalists.^{5,11,14}

ACKNOWLEDGMENTS

This work was supported by the NSF Nanosystems Engineering Research Center for Translational Applications of Nanoscale Multiferroic Systems (TANMS) under the Cooperative Agreement Award No. EEC-1160504.

APPENDIX A: MATH OPERATORS IN THE LINEARIZED LLG EQUATION AND MAGNETOSTRICTION STRAIN

Second order math operators $\underline{\underline{D}}_1$, $\underline{\underline{D}}_2$, and $\underline{\underline{D}}_3$ in Eq. (3) is given by

$$D_1 = \mu_0 \gamma \begin{bmatrix} 0 & -M_{eq3} & M_{eq2} \\ M_{eq3} & 0 & -M_{eq1} \\ -M_{eq2} & M_{eq1} & 0 \end{bmatrix}, \quad D_2 = \begin{bmatrix} 0 & -(\gamma\mu_0 H_{eq3} + i\alpha\omega M_{eq3}) & \gamma\mu_0 H_{eq2} + i\alpha\omega M_{eq2} \\ \gamma\mu_0 H_{eq3} + i\alpha\omega M_{eq3} & 0 & -(\gamma\mu_0 H_{eq1} + i\alpha\omega M_{eq1}) \\ -(\gamma\mu_0 H_{eq2} + i\alpha\omega M_{eq2}) & \gamma\mu_0 H_{eq1} + i\alpha\omega M_{eq1} & 0 \end{bmatrix},$$

$$D_3 = D_{ex} + D_{me} + D_{demag}, \quad D_{ex} = \frac{2A}{M_s \mu_0} \Delta \begin{bmatrix} 1 & & \\ & 1 & \\ & & 1 \end{bmatrix}, \quad D_{me} = -\frac{2}{M_s \mu_0} \begin{bmatrix} B_1 \varepsilon_{11} & 0 & B_2 \varepsilon_{13} \\ 0 & 0 & 0 \\ B_2 \varepsilon_{13} & 0 & B_1 \varepsilon_{33} \end{bmatrix},$$

$$D_{demag} = M_s \begin{bmatrix} N_{11} & N_{12} & N_{13} \\ N_{21} & N_{22} & N_{23} \\ N_{31} & N_{32} & N_{33} \end{bmatrix},$$

where M_{eqi} and H_{eqi} ($i=1,2,3$) are equilibrium magnetization and total effective field components along i direction. D_{ex} describes exchange term with A as exchange constant, and D_{me} is magnetoelastic field change due to magnetization deviation. D_{demag} is demagnetization field change due to magnetization deviation with N_{ij} as demagnetization factor obtained from FEA simulation. $\Delta = \nabla_{x,z}^2$ is math operator.

Feedback magnetostriction strain from magnetic system to piezoelectric system in Eq. (6) is given by²⁴

$$\varepsilon_{feedback} = \begin{bmatrix} -\frac{B_1}{(c_{11} - c_{12})} \left(m_1^2 - \frac{1}{3} \right) & -\frac{B_2}{c_{44}} m_1 m_2 & -\frac{B_2}{c_{44}} m_1 m_3 \\ -\frac{B_1}{(c_{11} - c_{12})} \left(m_2^2 - \frac{1}{3} \right) & & -\frac{B_2}{c_{44}} m_2 m_3 \\ sym & & -\frac{B_1}{(c_{11} - c_{12})} \left(m_3^2 - \frac{1}{3} \right) \end{bmatrix}.$$

APPENDIX B: PARAMETERS FOR Y-Z CUT LITHIUM NIOBATE

Parameters for Y-Z cut lithium niobate¹⁹

Density $\rho = 4647 \text{ kg/m}^3$.

Elastic Matrix

$$c_E = \begin{pmatrix} 2.424 & 0.752 & 0.752 & 0 & 0 & 0 \\ 0.752 & 2.03 & 0.573 & 0 & 0.085 & 0 \\ 0.752 & 0.573 & 2.03 & 0 & -0.085 & 0 \\ 0 & 0 & 0 & 0.752 & 0 & 0.085 \\ 0 & 0.085 & -0.085 & 0 & 0.595 & 0 \\ 0 & 0 & 0 & 0.085 & 0 & 0.595 \end{pmatrix} \times 10^{11} [\text{Pa}].$$

Coupling matrix

$$e = \begin{pmatrix} 1.33 & 0.23 & 0.23 & 0 & 0 & 0 \\ 0 & 0 & 0 & -2.5 & 0 & 3.7 \\ 0 & -2.5 & 2.5 & 0 & 3.7 & 0 \end{pmatrix} [\text{C/m}^2].$$

Relative permittivity

$$\xi = \begin{pmatrix} 28.7 & 0 & 0 \\ 0 & 85.2 & 0 \\ 0 & 0 & 85.2 \end{pmatrix}.$$

¹J. H. Moon, S. M. Seo, K. J. Lee, K. W. Kim, J. Ryu, H. W. Lee, R. D. McMichael, and M. D. Stiles, *Phys. Rev. B* **88**, 184404 (2013).

²D. Cortés-Ortuño and P. Landeros, *J. Phys. Condens. Matter* **25**, 156001 (2013).

³F. Garcia-Sanchez, P. Borys, R. Soucaille, J. P. Adam, R. L. Stamps, and J. Von Kim, *Phys. Rev. Lett.* **114**, 247206 (2015).

⁴A. V. Chumak, P. Pirro, A. A. Serga, M. P. Kostylev, R. L. Stamps, H. Schultheiss, K. Vogt, S. J. Hermsdoerfer, B. Laegel, P. A. Beck, and B. Hillebrands, *Appl. Phys. Lett.* **95**, 262508 (2009).

⁵M. Weiler, L. Dreher, C. Heeg, H. Huebl, R. Gross, M. S. Brandt, and S. T. B. Goennenwein, *Phys. Rev. Lett.* **106**, 117601 (2011).

⁶D. Labanowski, A. Jung, and S. Salahuddin, *Appl. Phys. Lett.* **108**, 22905 (2016).

⁷S. Bhuktare, A. Bose, H. Singh, and A. A. Tulapurkar, *Sci. Rep.* **7**, 840 (2017).

⁸P. G. Gowtham, D. Labanowski, and S. Salahuddin, *Phys. Rev. B - Condens. Matter Mater. Phys.* **94**, 014436 (2016).

⁹L. Thevenard, I. S. Camara, S. Majrab, M. Bernard, P. Rovillain, A. Lemaître, C. Gourdon, and J.-Y. Duquesne, *Phys. Rev. B* **93**, 134430 (2016).

¹⁰L. B. L. Thevenard, C. Gourdon, J. Y. Prieur, H. J. von Bardeleben, S. Vincent, and J.-Y. D. L. Largeau, *Phys. Rev. B* **90**, 94401 (2014).

¹¹P. G. Gowtham, G. E. Rowlands, and R. A. Buhrman, *J. Appl. Phys.* **118**, 183903 (2015).

¹²G. A. M. Gurevich and G. Alexander, *Magnetization Oscillations and Waves* (CRC Press, 1996).

¹³C. Chen, A. Barra, A. Mal, G. Carman, and A. Sepulveda, *Appl. Phys. Lett.* **110**, 072401 (2017).

¹⁴L. Dreher, M. Weiler, M. Pernpeintner, H. Huebl, R. Gross, M. Brandt, and S. Goennenwein, *Phys. Rev. B* **86**, 134415 (2012).

¹⁵L. Thevenard, J.-Y. Duquesne, E. Peronne, H. J. von Bardeleben, H. Jaffres, S. Ruttala, J.-M. George, A. Lemaître, and C. Gourdon, *Phys. Rev. B* **87**, 144402 (2013).

¹⁶V. Sampath, N. D'Souza, D. Bhattacharya, G. M. Atkinson, S. Bandyopadhyay, and J. Atulasimha, *Nano Lett.* **16**, 5681 (2016).

¹⁷T. L. Gilbert, *IEEE Trans. Magn.* **40**, 3443 (2004).

¹⁸N. Vukadinovic, *J. Magn. Magn. Mater.* **321**, 2074 (2009).

¹⁹D. Morgan, *Surface Acoustic Wave Filters: With Applications to Electronic Communications and Signal Processing* (Academic Press, 2007).

²⁰J. X. Zhang and L. Q. Chen, *Acta Mater.* **53**, 2845 (2005).

²¹N. P. A. V. Azovtsev, *Phys. Rev. B* **94**, 184401 (2016).

²²A. Kapelrud and A. Brataas, *Phys. Rev. Lett.* **111**, 097602 (2013).

²³N. Vukadinovic, J. Ben Youssef, V. Castel, and M. Labrune, *Phys. Rev. B - Condens. Matter Mater. Phys.* **79**, 184405 (2009).

²⁴B. D. Cullity and C. D. Graham, *Introduction to Magnetic Materials* (John Wiley & Sons, 2011).

²⁵J. R. Childress, C. L. Chien, and A. F. Jankowski, *Phys. Rev. B* **45**, 2855 (1992).

²⁶B. L. Zink, M. Manno, L. O'Brien, J. Lotze, M. Weiler, D. Bassett, S. J. Mason, S. T. B. Goennenwein, M. Johnson, and C. Leighton, *Phys. Rev. B - Condens. Matter Mater. Phys.* **93**, 184401 (2016).

²⁷O. Mosendz, J. E. Pearson, F. Y. Fradin, G. E. W. Bauer, S. D. Bader, and A. Hoffmann, *Phys. Rev. Lett.* **104**, 046601 (2010).

²⁸C. Kittel, *Introduction to Solid State Physics* (John Wiley & Sons, Inc., 2005).

²⁹J. L. Jackel, C. E. Rice, and J. J. Veselka, *Appl. Phys. Lett.* **41**, 607 (1982).

³⁰K. R. Parameswaran, R. K. Route, J. R. Kurz, R. V. Roussev, M. M. Fejer, and M. Fujimura, *Opt. Lett.* **27**, 179 (2002).

³¹S. Kakio, H. Shimizu, and Y. Nakagawa, *Electron. Commun. Jpn.* **95**, 19 (2012).

³²W. Zhang, M. B. Jungfleisch, W. Jiang, J. Sklenar, F. Y. Fradin, J. E. Pearson, J. B. Ketterson, and A. Hoffmann, *J. Appl. Phys.* **117**, 1 (2015).

³³A. Kamra, H. Keshtgar, P. Yan, and G. E. W. Bauer, *Phys. Rev. B - Condens. Matter Mater. Phys.* **91**, 104409 (2015).

³⁴K. Uchida, H. Adachi, T. An, H. Nakayama, M. Toda, B. Hillebrands, S. Maekawa, and E. Saitoh, *J. Appl. Phys.* **111**, 53903 (2012).

³⁵M. Weiler, H. Huebl, F. S. Goerg, F. D. Czeschka, R. Gross, and S. T. B. Goennenwein, *Phys. Rev. Lett.* **108**, 176601 (2012).